

Chapter 2: Literature Review

2.1: Hard Materials

2.1.1 Hardness

Hard materials are considered to be solids with a hardness value in the range of 8-10 on the Mohs scale of hardness¹. The accepted working definition of hardness is the resistance of a material to indentation by another material⁷. Hardness can partly be defined as the resistance of a material to plastic deformation. Although elastic deformation must occur before plastic deformation, the amount of elastic recovery by a hard material is usually insignificantly small with respect to the plastic deformation⁷. Generally materials only deform plastically when they are subjected to a shear stress and according to Frenkel analysis the yield stress of an ideal crystalline solid is directly proportional to its shear modulus⁸. Additionally, the shear stress needed for dislocation motion or multiplication and hence plastic deformation, is also proportional to the elastic shear modulus of the deformed material.

Also, in brittle materials crack formation always occurs during indentation. The formation of these cracks and the associated release of energy has a very large influence on the measured hardness of that material.

In most descriptions or theoretical appraisals of hardness investigators often describe the bulk and shear moduli for the material or phase under scrutiny⁹. There is some debate as to whether hardness is better described by the bulk or shear modulus. It has recently been argued by Teter *et al.* that in many hardness tests one measures plastic deformation which is more closely related to shear deformation¹⁰. A comparison of the shear and bulk moduli of a large number of materials was made by him with respect to the measured hardness of these materials. The results are presented in figure 2.1.1

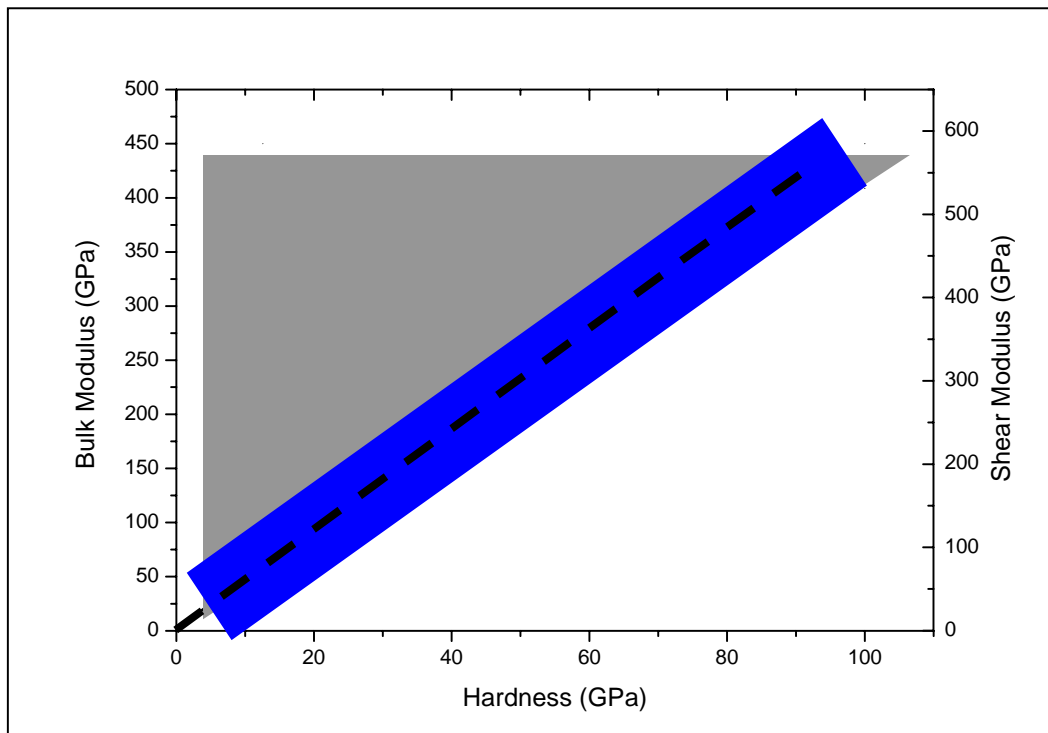


Figure 2.1.1: The scattering of the Vickers hardness measurements for various hard materials when compared with their corresponding bulk (grey area) and shear (blue area) moduli¹⁰

The determination of the hardness of almost any material is a challenging task, since a large number of factors, which can influence the results, have to be taken into account. These factors include the indenter geometry, testing load, time taken for indentation. Hardness values of different materials can only be compared with each other, if they are measured under exactly identical conditions¹¹.

Various testing methods are employed to determine the hardness of a material. Measurements can be done by indentation, scratch test, erosion and rebound methods. The discussion will be limited to indentation methods only. Specifically, Brinell, Knoop and Vickers hardness testing methods will be discussed. The indentation methods which have developed to determine hardness vary in indenter geometry and the definition of the contact area.

Brinell hardness is measured by indenting a material with a harder sphere. The corresponding Brinell hardness (H_B) is determined from the radius of the indent left behind. Knoop hardness (H_K) is determined by indenting a material with an elongated diamond indenter with a fixed ratio of the two diagonals. Measurements are taken by determining the length of the indent caused by the long diagonal. By rotating the indenter the associated anisotropy in the hardness measurement with respect to direction can be measured. Vickers hardness (H_V) measurements are performed using a square pyramidal shaped diamond indenter. The apex angle of the square pyramid is 136° . The hardness from such an indent is determined by finding the average length of the two diagonals. Vickers hardness measurements avoid variations due to anisotropy and the units are often quoted in kgmm^{-2} (Vickers numbers) or in the SI units of GPa.

In amongst other factors, hardness values are dependant on the magnitude of the load applied during testing. Valid hardness measurements require that the indentation be either very much less than the grain size (microhardness) in order to characterise the hardness of individual grains or the indentation load must result in indentations which are much larger than the grain size so as to ensure that the hardness of the polycrystals is determined (macrohardness), Figure 2.1.2 plots the common load-hardness relationship¹².

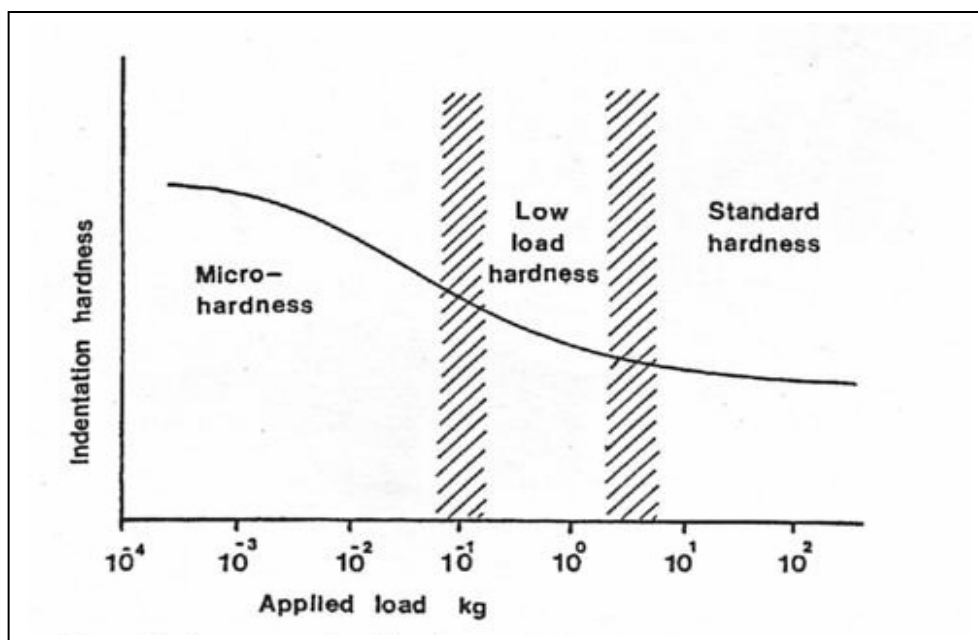


Figure 2.1.2: A common load-hardness relationship¹²

Hardness can be described as macrohardness, microhardness and nanohardness which are loosely defined for loads of larger than 1 kg, less than 200 g and less than 1 g respectively.

The most important material property factor that influences the hardness is the porosity. The grain size too has an effect. When reporting hardness values it is necessary to report the porosity and the grain size. Figure 2.1.3 illustrates the relationship between the grain size, porosity and Vickers hardness (at 1 kg load, H_{V1}) of an alumina ceramic.

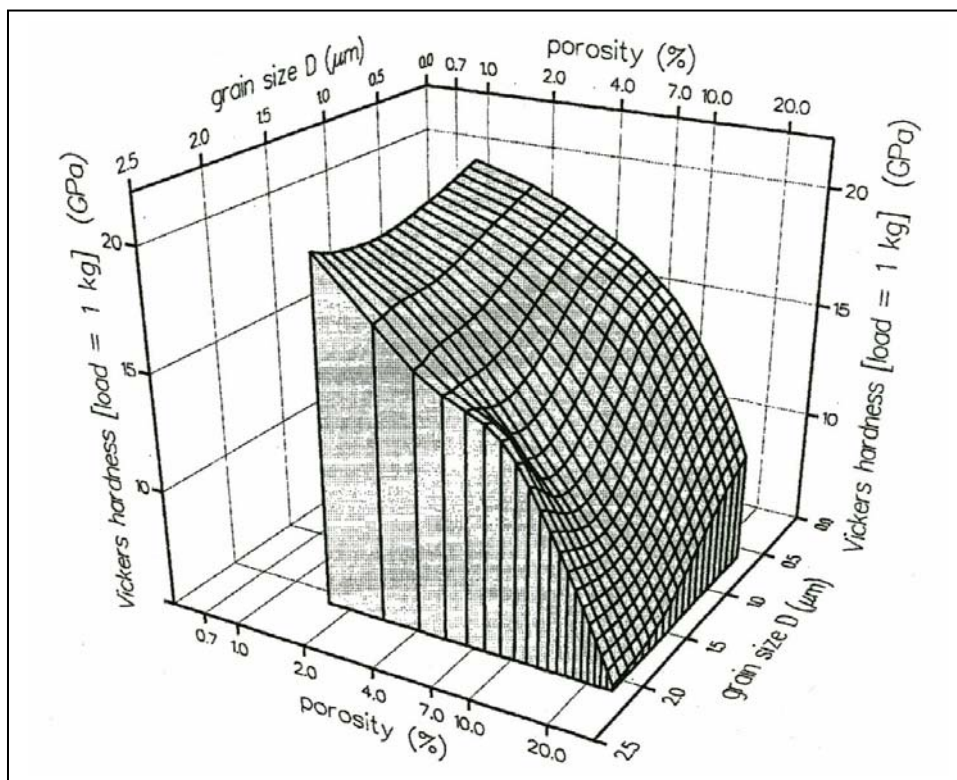


Figure 2.1.3: H_{V1} for a fine-grained sintered alumina ceramic prepared by a sol-gel approach starting with boehmite¹³

From figure 2.1.3 at high levels of porosity ($\approx 20\%$) the grain size has a pronounced effect on the hardness. Thus, as the average grain size decreases from 2.1-0.6 μm the H_{V1} value increases from about 5-10 GPa. The increase in hardness is attributed to the impedance of dislocation glide for smaller grain sizes. At lower levels of porosity ($\approx 1.5\%$) the effect of grain size (2.1-0.6 μm) is not as pronounced on the hardness (19-22 GPa)¹³

With such a large influence on the hardness for small changes in the porosity and with a further contribution from grain boundary phases to the inelastic deformation at an indentation site, it is obvious that many kinds of defects strongly influence the hardness. More specifically, in WC-Co it has been shown that as the content of the soft binder phase increases the hardness of the material decreases¹⁴ Hence, individual pores, clusters of pores, microcracks, grain boundary phases and other such defects within a material, located at the area of indentation, all promote the further penetration of an indenting body into that material¹⁵.

Hardness measurements are largely performed by indentation methods involving the use of a diamond indenter with a known geometry. Penetration depths increase as the load increases for brittle materials (and ductile materials). As the penetration depth increases, as a result of the increasing load, so to does the volume of material into which the stress is distributed beneath the indenter tip increase. This volume is referred to as the plastic zone. The radius of the plastic zone (R_{pl}) and the diagonal length (a) are related by equation 2.1¹⁶.

$$\frac{R_{pl}}{a} \approx 2 - 2.5 \quad 2.1$$

Thus, the radius of the plastic zone for microhardness measurements are often larger than 50 μm . Hence, hardness is strictly a bulk technique.

2.1.2: The traditional paradigm for a hard material

Hard materials can broadly be classified according to the type of chemical bonding in the material. Some metallic bonding such as TiB_2 and WC, covalent bonding with some ionic character Al_2O_3 and MgO and covalent bonding diamond, SiC, Si_3N_4 and c-BN. The hardest materials known in the literature are based on the family of covalently bonded materials. Diamond is the hardest known substance. It has a microhardness of between 70-90 GPa and is said to be ultra-hard. Ultra-hard materials are defined when a material's hardness exceeds 40 GPa¹. This realm of materials is sparsely populated with only diamond and c-BN (cubic-boronitride) occupying a

definite place in this realm. Some boron carbides and boron suboxides can form metastable phases that adopt ultra-hardness but these materials are not used extensively.

It is known that the hardest materials possess strong covalently bonded crystal structures of high symmetry. Hardness is a function of both the strength of the interatomic bonding and the rigidity of the lattice framework. Diamond is the hardest known bulk material and this is largely attributed to the strong covalent sp^3 bonding in a cubic lattice with tetrahedral coordination in a three dimensional network. The cF8 structure of diamond is also found in most of the other ultra-hard materials such as c-BN and several of the tetravalent metal carbides. Besides diamond, carbon has an additional modification known as graphite. Graphite has hexagonal symmetry and consists of the successive layering of rigid carbon planes bound together by weak Van der Waals forces. Therefore, the planes can move laterally with respect to each other, resulting in low hardness values. This lateral sliding of the graphite planes results in low friction coefficients. A similar situation exists for h-BN (hexagonal boronitride), which also has the cubic phase modification. The cubic phase modification has the diamond cF8 structure and is ultra-hard because of the largely covalently bonded BN that forms a three dimensional network crystal. Hence, the traditional paradigm of an ultra-hard material is that the atoms are largely covalently bonded in a three dimensional network structure with a simple unit cell and a high degree of symmetry.

2.2: Boride-based hard materials

One of the principle driving forces behind the development of boride-based hard materials is the better oxidation resistance of boride-based materials as compared with diamond-based materials. Boron-based hard materials of the binary or ternary systems B-C, B-N, B-O or B-C-N are generally more resistant to oxidation than diamond¹⁷. Diamond is prone to oxidation at temperatures in excess of 600°C in air whereas c-BN is resistant to oxidation up to 1100°C in air¹⁸.

2.2.1: Chemical bonding and structure types of some borides

Due to the high amount of covalent bonding in combination with small band gaps or even metal-like transport properties boride-based materials have very unique thermoelectric and hardness properties.

Chemical bonding in boron-based compounds is characterised by the two-electron-three-centre bond. The electrons are mostly delocalised and result in sp^2 hybridisation which leads to the plane B_3X_3 hexagonal structural unit found in BN, B_2O_3 and to the B_3 triangle which forms the typical five-fold symmetric icosahedrons of elemental boron which are composed of 12 B atoms, figure 2.2.1. Boron compounds may contain ionic, metallic and covalent bonds.

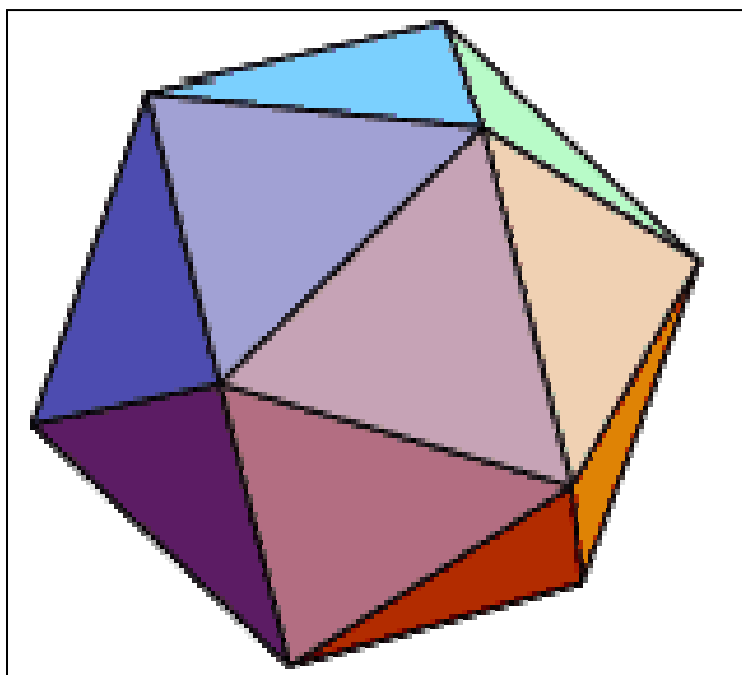


Figure 2.2.1: A typical five-fold symmetric icosahedron

As introduced earlier boron forms the basis of several important materials with a variety of structural phases. The main building block in these materials are the boron icosahedra. Boron carbide (B_4C), which crystallises in the trigonal-rhombohedral space group $R3m$, consists of C rods linking the boron icosahedra¹⁹. The C rod linkage model has been the subject of much debate and an additional structure in which C atoms actually occupy sites within the icosahedra in a polar structure has been

supported by electronic structure calculations²⁰. Both of these structures are presented in figure 2.2.2.

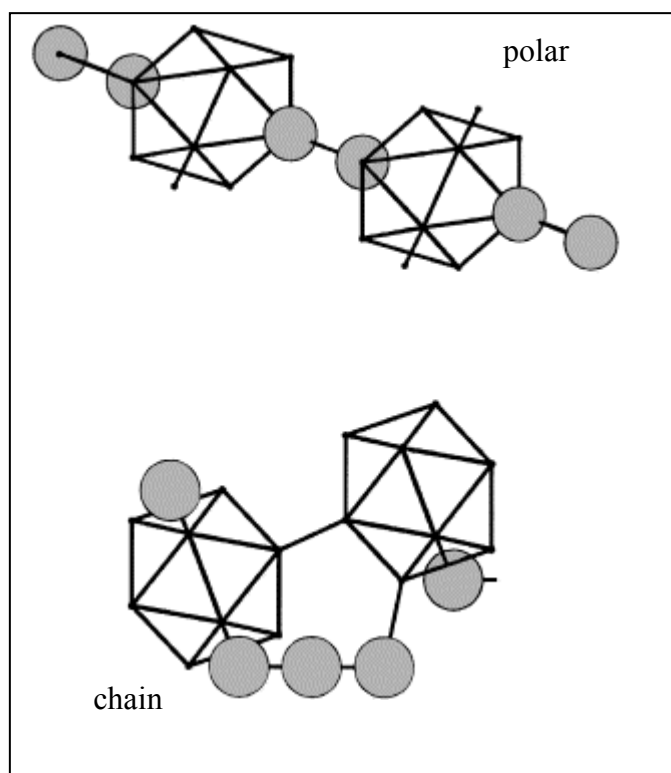


Figure 2.2.2: The structure of B_4C in the chain or polar structures²¹

2.2.2: The structure of $AlMgB_{14}$

The material under scrutiny in this work is $AlMgB_{14}$ for reasons that were addressed in chapter 1. The structure of $AlMgB_{14}$ was first determined by Matkovich *et al*³. Single crystals of $AlMgB_{14}$ were grown in alumina crucibles from aluminium rich fluxes with starting atomic percent compositions of 2:1:14 respectively. The elemental compositions were heated to 900°C and held at this temperature for 6 hours under a constant flow of N_2 and the single crystals were obtained by washing the product with concentrated hydrochloric acid. A residue of small black crystals was isolated and shown to be a single phase of approximate composition $AlMgB_{14}$. The crystal had a density of about 2.60 gcm^{-3} .

The unit cell is orthorhombic with lattice parameters $a = 10.313$, $b = 8.115$, $c = 5.848$ Å. This structure is based on B_{12} icosahedra linked together by Al and Mg.

“Four icosahedral B_{12} groups centred at 000 , $0\frac{1}{2}\frac{1}{2}$, $\frac{1}{2}00$ and $\frac{1}{2}\frac{1}{2}\frac{1}{2}$ are present. The icosahedra are oriented in such a way that two of the apical atoms lie along the a axis and a mirror plane of the icosahedra lies in the ab plane. The aluminium atoms occupy a fourfold position at $\frac{1}{4}\frac{3}{4}\frac{1}{4}$ and magnesium occupies a fourfold position at $\frac{1}{4}y0$ ($y = 0.359$). Partial occupancy is indicated for both metal atoms. The extra icosahedral boron atoms occupy the eightfold position at $xy0$ ($x = 0.152$ and $y = 0.622$). Forty boron atoms have six boron neighbours and two metal neighbours. Eight boron atoms have six boron neighbours, and eight (extra icosahedral) boron atoms have four boron and three metal neighbours. Aluminium has twelve and magnesium has fourteen neighbours. The B_{12} icosahedral units in $AlMgB_{14}$ are arranged in distorted closest packed layers which are stacked directly one above the other. The unit cell contains a total of 64 atoms and has the space group $Imma^3$ ”. Figure 2.2.3 is a presentation of the crystal structure as a projection on the ab plane.

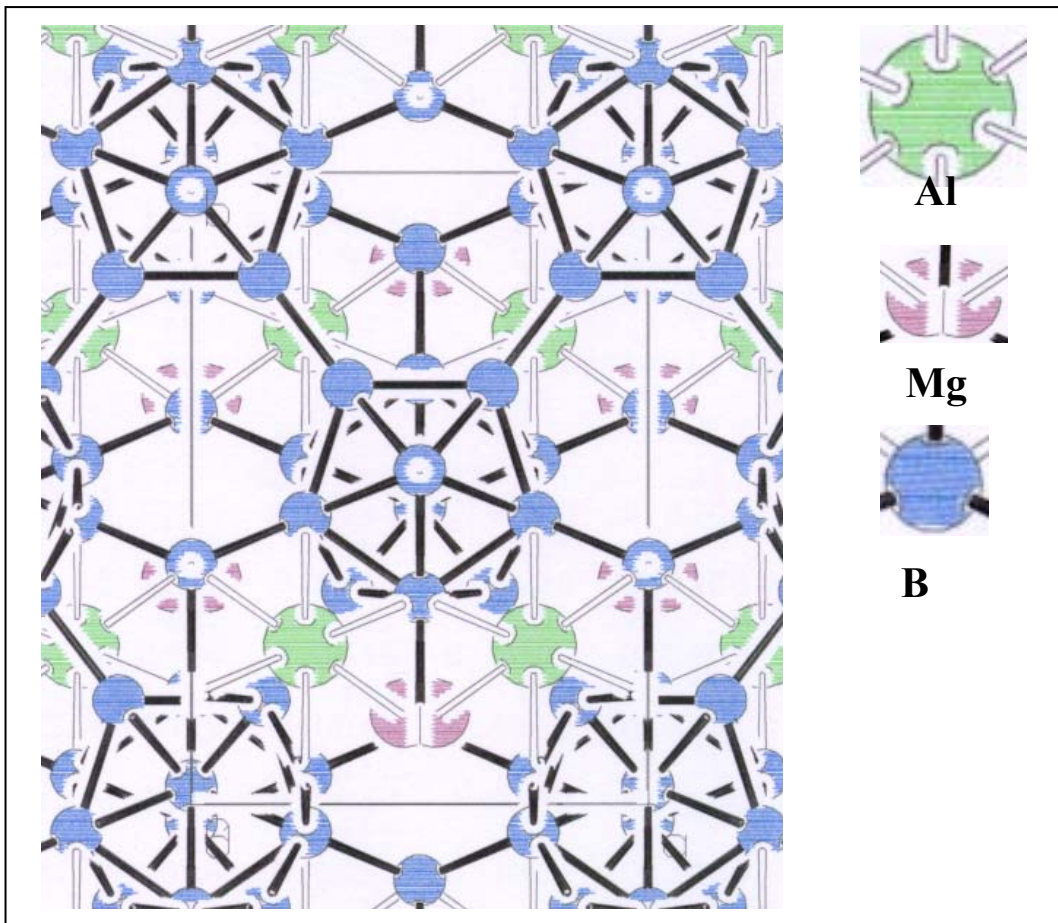


Figure 2.2.3: Crystal structure of $AlMgB_{14}$ projection on the ab plane

A refinement to the structure proposed by Matkovich *et al.* was put forward in the literature by Higashi²². Higashi produced AlMgB₁₄ by heating an atomic ratio mixture of 31:1:6 respectively of the elemental powders in an inert atmosphere for 1 hour to 1500°C in an alumina crucible. The crystals were obtained from the solidified mixture by dissolving the excess aluminium in hot hydrochloric acid. The lattice constants were determined from 20 reflections within the 2θ range 70°-90°.

Higashi found that the magnesium metal sites are split and that the aluminium site at $\frac{1}{4}^3\frac{1}{4}$ is partially occupied by aluminium atoms (75% occupancy) and the magnesium site at $0y^3\frac{1}{4}$ ($y = 0.359$) is partially occupied by both magnesium (50%) and aluminium atoms (25%). Thus, the metal occupancy in the structure for aluminium is 74.8% and 78% for magnesium. The space group was thus modified to *Imam*. Hence, the chemical formula proposed by Higashi's work for AlMgB₁₄ is Al_{0.75}Mg_{0.78}B₁₄²².

2.2.3: The production of dense polycrystalline AlMgB₁₄ and associated impurity phases

The synthesis of AlMgB₁₄ by Cook involved the high energy milling of the elemental powders in hardened stainless steel vials for 12 hours in a vibraspex mill or planetary milling for times between 50-100 hours. Additionally, pieces of Al and Mg were used for milling as opposed to powders of these metals in an attempt to limit the amount of oxide phases in the starting Al and Mg constituents².

After milling, the loose powder was removed from the vial and 1 g quantities were hot pressed at temperatures ranging from 1400°C to 1500°C, 1 hour soak time and 103-140 MPa under a He atmosphere. After hot-pressing the samples were ground and polished using diamond embedded steel grinding plates and 1 μm diamond grinding slurries. The density of the compacts so produced was 2.59 gcm⁻³.

Additional studies on this material involved the characterisation of the impurity phases. Because milling took place in a hardened stainless steel vial with hardened stainless steel balls Fe is introduced into the elemental powders during the milling cycle. The Fe reacts with either the boron or AlMgB₁₄, according to reactions 2.2. and 2.3 and forms FeB.



X represents some other lower boron rich solid (e.g. AlB_{12} , AlB_{10}) that can be formed in addition to $(\text{Al,Mg})\text{B}_2$.

The second reaction was not suggested by Cook and no XRD data was provided in the publication and so the proposal that is being made would have to be verified.

The most common impurity phase observed by Cook *et al.* was the spinel phase MgAl_2O_4 . An additional impurity phase detected by them was Fe_2O_3 . They suggested that the spinel phase formed as a result of the presence of O in the initial elemental constituents, adsorbed atmospheric O and H_2O . They also reported that the lowest impurity content (an unknown composition containing MgAl_2O_4 , Fe_2O_3 and FeB) possible in hot-pressed samples was about 2 vol.% and that using powders subjected to longer exposure times to the atmosphere was about 10 vol.%. Using the density of MgAl_2O_4 (3.6 gcm^{-3})²³ and assuming that all the impurity phase is the spinel the minimum and maximum vol.% translate to 3 and 13 wt.% respectively.

2.2.4: Electrical, Thermal and Magnetic Properties of AlMgB_{14}

Prior to the discovery of the high hardness of AlMgB_{14} by the Ames group, previous studies on the AlMgB_{14} compound were primarily concerned with the optical and electronic and thermoelectric properties of the orthorhombic AlMgB_{14} -type borides^{24, 25 & 26}. Based on the work by Bairamashvili²⁴ simultaneous increases in the electrical conductivity and the thermoelectric power occurred over a wide temperature range, which is characteristic of a hopping conduction mechanism. The measurement of the Seebeck coefficient for single phase AlMgB_{14} measured by Werheit²⁵ and Takeda²⁶ were $-6500 \mu\text{VK}^{-1}$ and $+500 \mu\text{VK}^{-1}$ respectively. These values are substantially different and no reason has been offered for this discrepancy. Werheit also measured the electrical resistivity of $50 \Omega\text{m}$ for single crystal, high purity AlMgB_{14} .

Resistivity measurements were performed on polycrystalline AlMgB₁₄ by Cook *et al.* The results are presented in figure 2.2.4.

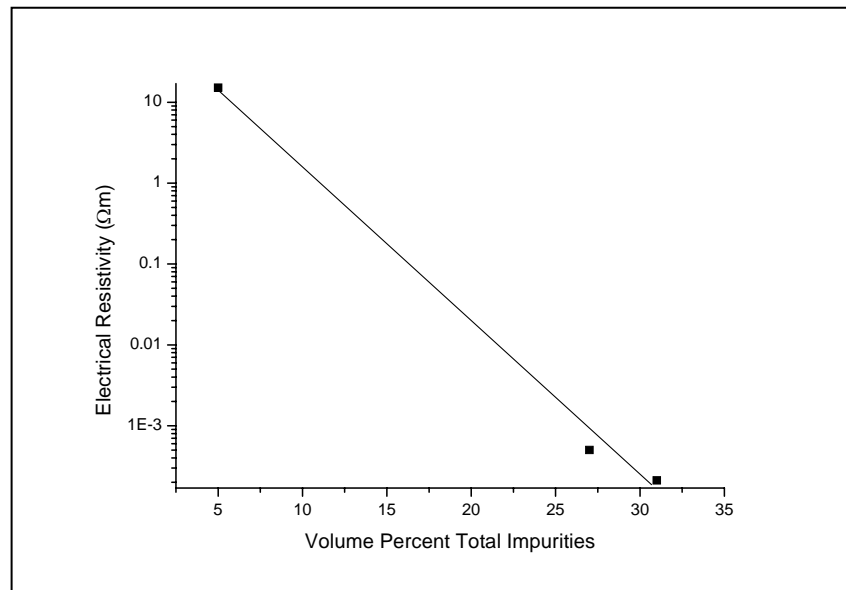


Figure 2.2.5 b: A plot of the electrical resistivity in AlMgB₁₄ as a function of the total volume percent of Al₂MgO₄, Fe₃O₄ and FeB impurity phases²⁷

Because of the lower conductivity of the impurity phase the resistivity decreased by 5 orders of magnitude as the impurity content increased. Determination of the Hall coefficient from the resistivity measurements suggested that these materials are n-type semiconductors. The resistivity of the polycrystalline AlMgB₁₄ samples with different impurity levels range from as low as $7 \times 10^{-5} \Omega\text{m}$ to $28 \Omega\text{m}$ which is lower than the value of $50 \Omega\text{m}$ determined by Werheit for single crystal AlMgB₁₄. Theoretical calculations on the electronic states of AlMgB₁₄ have shown that the Fermi level lies in states above a band gap of about 1 eV for the ideal AlMgB₁₄ crystal. With the observed 25% vacancies in the Al and Mg sites, calculations indicate that the Fermi level falls below the gap, near the top of a broad set of bands having predominately boron character. The vacancies lower the total energy per atom below that of the 64 atoms per unit cell. Hence, the ideal 62 atom structure with ordered vacancies should be metallic. Electron scattering near the top of the occupied boron bands at the Fermi level can be very high and some of the electronic states could become localised due to the disordered vacancies. Thus, one expects transport properties such as electrical

resistivity to be sensitive to sample preparation methods which have a large impact on the ordering of the vacancies²⁸.

Magnetic susceptibility X and magnetisation M versus temperature, and isothermal M versus the magnetic field H studies of dense AlMgB_{14} was carried out by Hill *et al.* in search of superconductivity or ferromagnetism in this compound²⁹. Due to the presence of the impurity phases of MgAl_2O_4 and FeB , measurements could not be performed on pure AlMgB_{14} prepared in the manner described by Cook *et al.* The purifying hot-acid wash used both by Matkovich and Higashi did not significantly alter the phase composition of the samples used when testing the magnetic properties of AlMgB_{14} .

Hill *et al.* concluded that pure AlMgB_{14} is neither a superconductor nor a ferromagnet above 1.8 K and exhibits temperature-independent diamagnetism from 1.8 K up to room temperature. The ferromagnetism observed in the hot-pressed samples is likely due to the Fe impurities abraded from the stainless steel mills used to mix the starting materials prior to hot-pressing the samples.

2.2.5: The microhardness of polycrystalline AlMgB_{14}

The microhardness of single crystal AlMgB_{14} was determined by Higashi to be between 27.4 and 28.3 GPa²². The findings of Cook *et al.* found the microhardness of AlMgB_{14} prepared by hot-pressing elemental atomic compositions of 1:1:14 respectively to be between 32-35 GPa². The increased hardness is not unusual since the measurement by the Ames group was done on a polycrystalline material and probably with a very low load. Due to the impedance of dislocation movement as a result of polycrystalline samples, largely dependant on the grain size of the polycrystals, the hardness of polycrystalline samples is usually slightly higher than the hardness of the corresponding single crystal¹⁵.

The presence of the impurity phases were deleterious to the microhardness of polycrystalline AlMgB_{14} prepared by Cook *et al.*, as shown in figure 2.2.5²⁷.

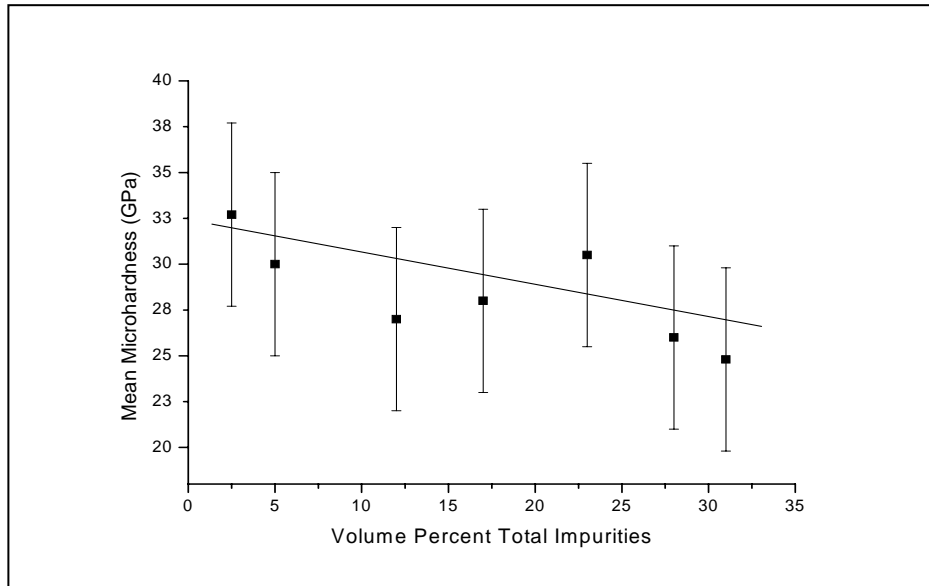


Figure 2.2.5: A plot of the mean microhardness as a function of the total volume percent of Al_2MgO_4 , Fe_3O_4 and FeB impurity phases in AlMgB_{14} . Error bars indicate one standard deviation. No load has been specified for the microhardness measurement²⁷

Even though the boron materials based on the B_{12} icosahedra are usually hard, the low symmetry of the orthorhombic crystal structure for AlMgB_{14} coupled with the complicated unit cell (64 atoms) and the fact that the Al-B and Al-Mg bonds in AlMgB_{14} are most likely less covalent than both C-C and B-N bonds contradicts the traditional paradigm of an ultra-hard material 1. In spite of this, polycrystalline AlMgB_{14} has high hardness and furthermore when alloyed with 5 wt.% Si or 30 wt.% TiB_2 the hardness of polycrystalline AlMgB_{14} is further enhanced. The microhardness of AlMgB_{14} and a few other hard materials together with their bulk and shear moduli (when known) are tabulated in table 2.1.

TABLE 2.1: Density, hardness, bulk and shear moduli of selected hard materials²

Material	Density (gcm⁻³)	H_{V1} (GPa)	Bulk Modulus (GPa)	Shear Modulus (GPa)
C (diamond)	3.52	70	443	535
c-BN	3.48	45-50	400	409
c-C ₃ N ₄	†	40-55	496	332
SiC	3.22	24-28	226	196
B ₄ C	2.52	30-50	250	-
TiB ₂	4.50	30-33	244	263
WC	15.72	23-30	421	-
TiC	4.93	28-29	241	188
AlB ₁₂	2.58	26	-	-
Si ₃ N ₄	3.19	17-21	249	123
*AlMgB ₁₄	2.66	32-35	212 ²⁶ 208-213 ²⁸	231 ²⁶
*AlMgB ₁₄ + Si	2.67	35-40	205 ²⁸	-
*AlMgB ₁₄ + TiB ₂	2.70	40-46	-	-

† presently available in quantities too small to permit measurement of bulk density

* load not specified

Cook *et al* suggested that the increase in hardness due to the addition of Si may be that the Si atoms substitute for Al in the orthorhombic unit cell or occupy some of the vacant Al or Mg sites present in the Al and Mg deficient substoichiometric unit cell. Thus, the smaller Si atoms might give rise to a slightly higher occupancy. Hence, the inter-icosahedral bonding might be stronger, leading to a more rigid unit cell. Moreover, the additional electron provided by the Si would be expected to form an additional bond with the boron icosahedra. Additionally, Cook suggested that microstructural refinement may also contribute to the increased hardness. Cook was unable to explain the resulting ultra-hard composite formed by the addition of 30 wt.% TiB₂ to AlMgB₁₄ and Cook argued that any clarifying explanation would have to account for the numerous compounds that may form at the AlMgB₁₄-TiB₂ interface. Cook insisted that in order to resolve the questions raised from the increased hardness of AlMgB₁₄ as a result of the Si and TiB₂ additions structure determinations

of the composites along with theoretical calculations of the relevant bonding energies would need to be done. Such calculations have since been concluded by independent researchers and the results will be presented in section 2.2.6.

2.2.6: Elastic constants of polycrystalline $AlMgB_{14}$

As discussed in section 2.1.1, elastic constants are believed to be related to the strength of a material. The bulk and shear moduli are frequently calculated for materials when investigating their hardness. It has been shown by Teter the shear modulus exhibits a better correlation with the measured hardness than the bulk modulus¹⁰.

The correlation of the shear moduli calculated by Lee *et al.* with the observed microhardness is shown in figure 2.2.6²⁸.

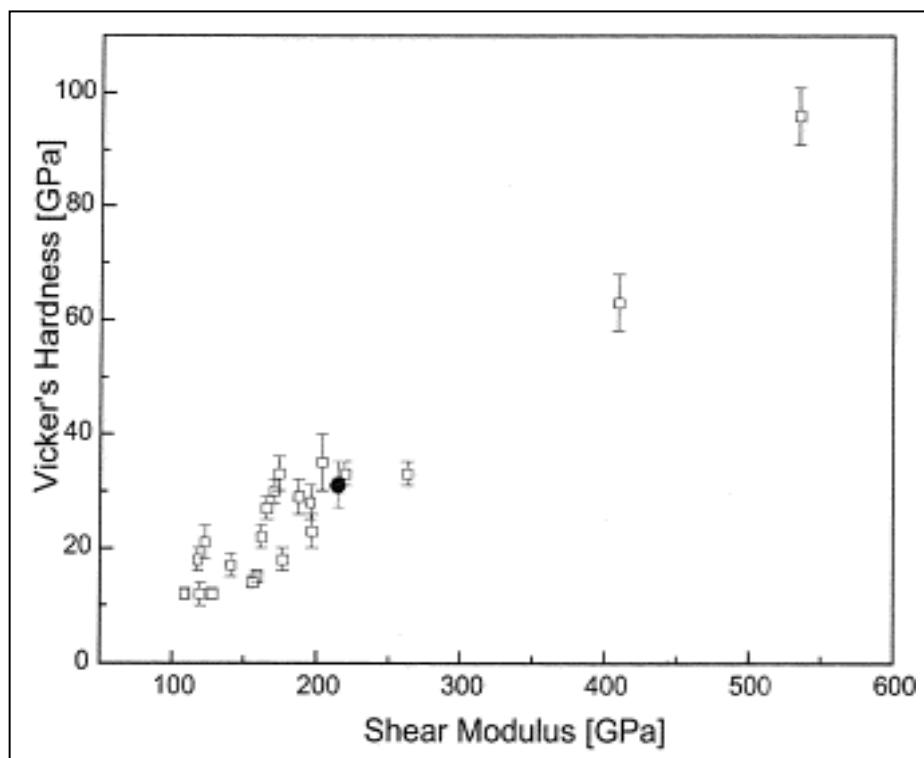


Figure 2.2.6: Plot of microhardness (H_{V1}) vs. shear modulus for various materials¹⁰. The filled circle shows the position of $AlMgB_{14}$ (no load has been specified for this measurement)²⁸

The enhancement of the hardness of AlMgB_{14} by the addition of Si has been dealt with in detail by Lowther⁴. It was tentatively suggested by Cook that the enhancement of the hardness of AlMgB_{14} could be a result of the substitution of one or more of the Al sites with Si which yielded a higher occupancy and thus ‘stiffened’ the lattice of AlMgB_{14} . Figure 2.2.7 is a different orientation of part of the AlMgB_{14} crystal structure.

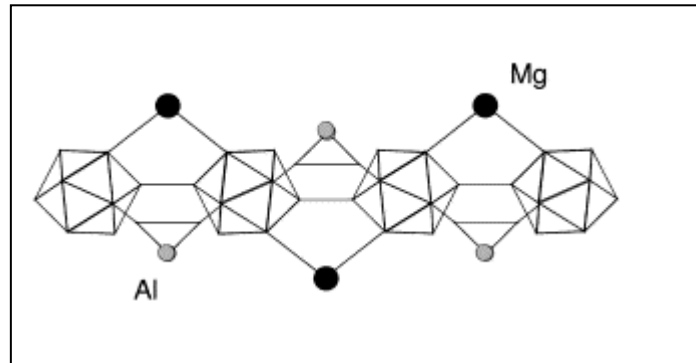


Figure 2.2.7: Part of the structure of AlMgB_{14} showing the locations of Al and Mg relative to the B icosahedra⁴

It is clear from figure 2.2.7 that Al is more closely associated with the B icosahedra than Mg. The bulk modulus of this material was then calculated based on Cook’s suggestion that Si will substitute directly for Al. Based on the electronic charge density in the material it was shown that there is no bonding between Mg and B. Furthermore, there was very little evidence of a strong chemical bond between Al or Si and the B icosahedra. Thus, the presence of Al or Si within the *Imam* structure of the B icosahedra has little effect on the chemical bonding of the B icosahedra.

Bulk moduli calculations for AlMgB_{14} and the Si substituted AlMgB_{14} indicate that the bulk moduli of both materials is lower than that of B_4C . Furthermore, Lazzari *et al.* calculated the bulk modulus of an isolated B icosahedron to be 297 GPa which is higher than B_4C concluding therefore that the upper limit of the bulk modulus of any B icosahedral based structure to be upper-bounded by the bulk modulus of the icosahedron unit itself²⁰. Hence, the bulk modulus of any new material, with different linkage atoms, based on boron icosahedra will not result in the enhancement of the bulk modulus of the boron icosahedron itself.

It has been suggested in a recent publication by Clerk and Leadbitter that the mechanical concept of hardness relates to the shear elastic moduli and a quantity termed the chemical hardness³¹. The chemical hardness is the second derivative of the total energy of the system with respect to the electron population. Hence, this term will be dependant on changes of the electronic structure that lie near to the Fermi energy of the material. As argued by Lee²⁸ AlMgB₁₄ has a Fermi level located within an energy band lying above an energy gap and Lowther⁴ showed that the Fermi level of B₄C lies in the energy gap and this difference between AlMgB₁₄ and B₄C may be influencing the chemical hardness of the material rather than affecting the overall bonding within the structure. Thus, it would be of interest to quantify the chemical hardness factor for boron icosahedra in order to more fully understand the reported ultra-hard nature of AlMgB₁₄.

2.2.7: Thermal Expansion of polycrystalline AlMgB₁₄

TABLE 2.2: Coefficient of thermal expansion of some important hard materials

Material	Coefficient of thermal expansion (x 10 ⁻⁶ K ⁻¹)
AlMgB ₁₄	9 ²⁸
B ₄ C	6 ³⁰
TiB ₂	7.8 ³⁰
SiC	5.6 ³⁰
W ₂ B ₅	7.8 ³⁰
WC	6 ³⁰

The coefficient of thermal expansion has been determined for polycrystalline AlMgB₁₄ prepared by the method developed by Cook *et al*². The coefficient of thermal expansion was measured by dilatometry and by high temperature X-ray diffraction using synchrotron radiation³⁰. The coefficient of thermal expansion over the temperature range 298 K to 1373 K was determined to be 9 x 10⁻⁶ K⁻¹, which is relatively close to the value of 8.3 x 10⁻⁶ K⁻¹ for pure B. The anisotropy of the coefficient of thermal expansion appeared to be relatively small for AlMgB₁₄.

From an engineering perspective, a coefficient of thermal expansion of $9 \times 10^{-6} \text{ K}^{-1}$ is a favourable value for the possible use of AlMgB_{14} as a hard coating. The value is similar to the coefficient of thermal expansion of several widely used materials such as steel ($11.7 \times 10^{-6} \text{ K}^{-1}$), Ti ($8.6 \times 10^{-6} \text{ K}^{-1}$) and concrete ($10\text{-}13 \times 10^{-6} \text{ K}^{-1}$).

In composite materials the thermal expansion mismatch has a large influence on the internal stresses of that composite which usually results in an increased fracture toughness.

The enhancement of the fracture toughness of a material due to crack deflection around embedded particles in a matrix with dissimilar thermal expansion coefficients is known to be true³³. The reason for the enhancement is due to the formation of microcracks around the embedded material with a larger thermal expansion coefficient than the matrix. The formation of the microcracks occurs as a result of the generation of residual stresses around the embedded particles during cooling. Figure 2.2.8 shows just such a deflection mechanism in operation for a $\text{TiB}_2\text{-B}_4\text{C}$ composite prepared by reaction hot-pressing at 2000°C , 1 hour soak time and 50 MPa ³⁴. Such a mechanism has also been observed in a SiC-TiB_2 composite³⁵.

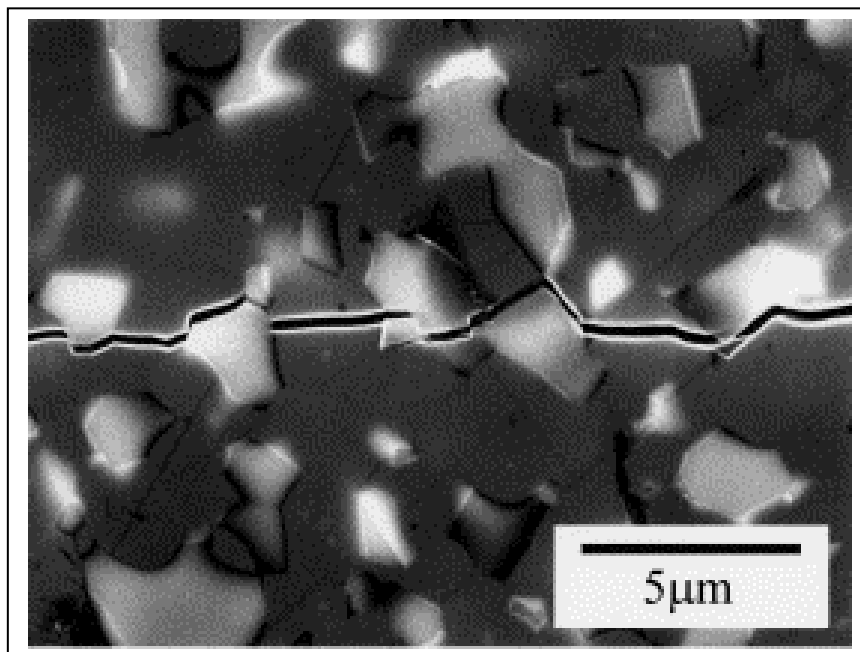


Figure 2.2.8: Crack deflection around TiB_2 particles in a B_4C matrix³⁴

In light of the previous arguments, the thermal expansion coefficients introduced in table 2.2 indicate that AlMgB_{14} may possibly have sufficient thermal expansion mismatch when alloyed with TiB_2 or W_2B_5 to lead to micro-cracking and subsequent enhancement of the fracture toughness.

The absolute difference of the coefficient of linear thermal expansion between AlMgB_{14} and TiB_2 and W_2B_5 is 1.2 compared to 1.8 for those composites based on a B_4C matrix. Hence, the opportunity exists to utilise either TiB_2 or W_2B_5 or a combination of both to enhance the fracture toughness of the composite material based on AlMgB_{14} through crack deflection.

2.2.8: Applications of AlMgB_{14}

Compared with diamond and c-BN, AlMgB_{14} is a thermodynamically stable material with reasonable electrical conductivity, high chemical stability and low density³⁶. The projected cost of manufacture of the boride is 10% that of diamond and c-BN. AlMgB_{14} based materials appear to be congruently melting/evaporating, which would allow them to be processed with techniques such as pulsed laser deposition³⁶.

AlMgB_{14} materials have been successfully used as coating materials on WC/Co cutting tool inserts³⁶. Although EDS analysis of coating layers confirmed that the elements Al, Mg and B were roughly in the correct stoichiometric amounts (1:1:14) no thin film X-ray diffraction measurements had been done on the coatings to confirm if the coating layer has preserved the orthorhombic unit cell of AlMgB_{14} .

SEM images of the fractured surface of an AlMgB_{14} coated WC/Co tool insert indicate firstly that AlMgB_{14} 's fracture surface is smooth indicating that it undergoes brittle fracture, which is consistent with the conventional mode of fracture for hard materials³⁶. Secondly, that the AlMgB_{14} bonds very well to the substrate³⁶. The coating is uniform, dense and adherent even after brittle fracture³⁶. The strong adherence has been attributed to the high speed of colliding species that generate a pressure pulse of as high as 1 MPa³⁷.

Coatings of AlMgB₁₄, TiB₂ and a composite coating of AlMgB₁₄ and TiB₂ were tested in turning AISI 1045 steel bars. The coated tools provided consistent reductions in wear with cutting time although the percentages of wear reduction decreased with an increase in cutting time. The average percentage reduction in wear was about 12%³⁶. The applied coating was as thin as 0.5 μm and it has been found that as the coating thickness increases the wear performance improves³⁸.

The improvements in wear reduction are modest in TiB₂ coatings but are significant in multilayer, composite AlMgB₁₄/TiB₂ coatings, figure 2.2.9. One of the reasons offered by the group is that the difference in the thermal expansion coefficients between TiB₂ and WC result in a poorer adherence of the TiB₂ coating to the WC/Co tool³⁵. If one looks at table 2.2 then it is most likely not the case that poor adherence due to thermal mismatch (9 and 7.8 x10⁻⁶K⁻¹ respectively) is the reason for AlMgB₁₄+TiB₂ coatings out performing TiB₂ coatings.

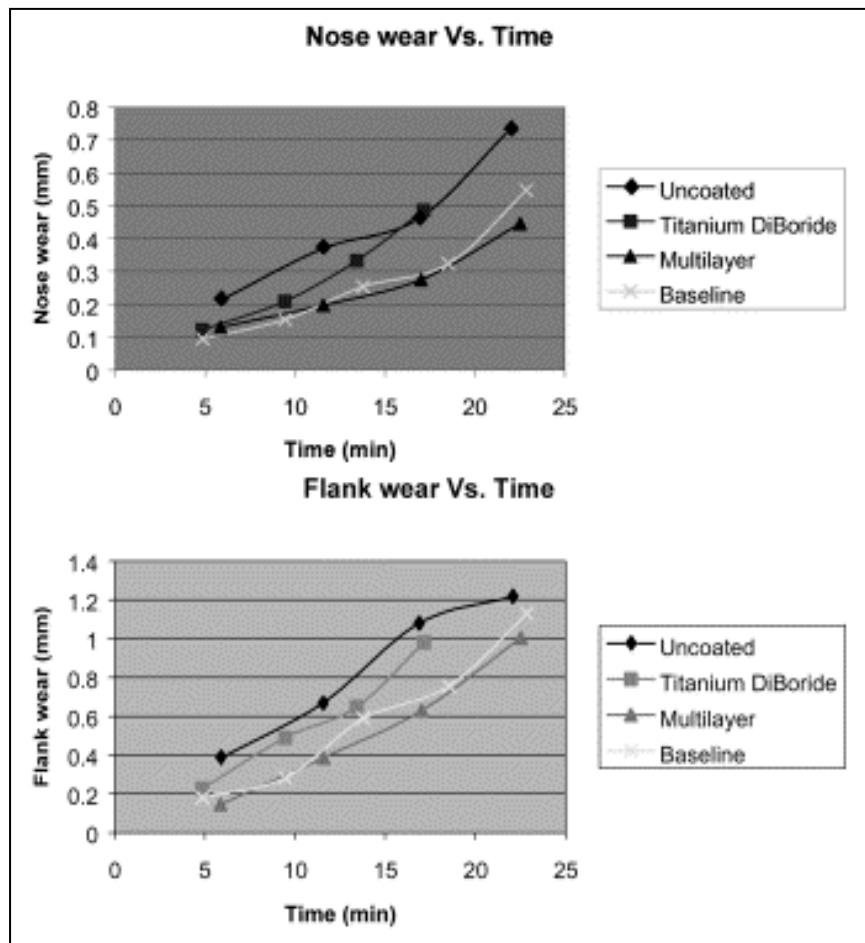


Figure 2.2.9: Flank and nose wear vs. cutting time for uncoated and coated tools in dry machining³⁶

The baseline material referred to in figure 2.2.9 is when the tool is coated with AlMgB_{14} .

2.2.9: Binary and Ternary Phase systems of interest

In order to complete the picture it is necessary to deal with those binary and ternary phase systems that are of prime importance. As described in the introductory chapter a detailed investigation of the behaviour of the solid solution boundary is presented in chapter 4. For purposes of convenience the phase systems for the Al-B, Mg-B and Al-Mg binaries and Al-Mg-B ternary phase diagrams are presented in the introductory remarks of that chapter, see section 4.1.

Furthermore, the remarkable improvement in the hardness of AlMgB_{14} by the addition of 5 wt.% and 30 wt.% TiB_2 warranted further investigation and composites were prepared with the additions of Si, TiB_2 , TiC, TiN, TiCN and WC, the results of which are presented in chapter 6. Therefore, a survey of the ternary systems Ti-C-B, Ti-N-B and W-C-B will be addressed in section 6.1.